Nanoscale

PAPER

View Article Online
View Journal | View Issue

Cite this: *Nanoscale*, 2022, **14**, 7538

Boosting photocatalytic CO_2 reduction *via* Schottky junction with ZnCr layered double hydroxide nanoflakes aggregated on 2D $Ti_3C_2T_x$ cocatalyst†

Boye Zhou,[a,b] Yong Yang,*[c] Zhengchu Liu,[a,b] Niandu Wu,[a] Yuxiang Yan,[a] Zhao Wenhua,[a] Huichao He,[d] Jun Du,[a] Yongcai Zhang,[e] Yong Zhou*[a,b,f] and Zhigang Zou[a,b,f]

Received 15th March 2022,
Accepted 4th May 2022

DOI: 10.1039/d2nr01448c

rsc.li/nanoscale

Designing efficient photocatalysts is vital for the photoreduction of CO_2 to produce solar fuels, helping to alleviate issues of fossil fuel depletion and global warming. In this work, a novel ZnCr-LDH/$Ti_3C_2T_x$ Schottky junction is successfully synthesized using an *in situ* coprecipitation method. ZnCr-LDH nanoflakes collectively grow on the surface of $Ti_3C_2T_x$ MXene nanosheets. When using $Ti_3C_2T_x$ MXene as a cocatalyst in the prepared heterojunction, the light absorption intensity, photo-induced electron separation and migration efficiency increase. As a result, the composite ZnCr-LDH/$Ti_3C_2T_x$ results in significant improvement in the performance of photocatalytic CO_2 reduction under simulated solar irradiation. The optimized sample ZCTC25 has the highest photocatalytic CO_2 reduction rates of 122.45 μmol g^{-1} CO and 19.95 μmol g^{-1} CH_4 (after 6 h of irradiation). These values are approximately 2.65 times higher than those of pristine ZnCr-LDH. The product selectivity towards CO is 86%. This work provides a new method for the construction of novel 2D semiconductor photocatalysts and enriches the application of an unusual type of layered double hydroxides in the photoreduction of CO_2.

Introduction

The consumption of fossil fuels and continuous CO_2 emissions have caused a global energy crisis and environmental issues. The photocatalytic reduction of CO_2 into hydrocarbon fuels using solar energy is recognized as a harmless solution to decrease the level of atmospheric CO_2 and achieve carbon neutrality.[1] However, the efficiency of the photoreduction process is limited by the inherent inertness of CO_2 molecules and complex reduction pathways involving multiple electrons and protons.[2] The key to solving these problems is to design and develop highly efficient photocatalysts. A popular approach is to build up a two-dimensional (2D) thin-layered photocatalyst system with a suitable bandgap and band edge position. Because of its large specific surface area and abundant surface atoms with unsaturated coordination, the light-harvesting ability significantly improves. The ultrathin thickness can shorten the diffusion distance from the interior to the surface, and therefore accelerate the charge transfer process and reduce the recombination of photoexcited charge carriers in the body. Additionally, the high ratio of exposed surface atoms gives the thin layered photocatalyst more active sites for the desired reactions.[3,4] However, no 2D thin-layered photocatalyst can achieve a high photocatalytic efficiency without further modification. One approach to achieving the optimal performance is assembling different materials in a heterostructure to create a cooperative effect.

Layered double hydroxides (LDHs), 2D anionic intercalated materials with the general formula $[M^{2+}_{1-x}M^{3+}_{x}(OH)_2]$

[a]*National Laboratory of Solid State Microstructures, Collaborative Innovation Center of Advanced Microstructures, School of Physics, Nanjing University, Nanjing 210093, P. R. China. E-mail: zhouyong1999@nju.edu.cn*
[b]*Eco-Materials and Renewable Energy Research Center (ERERC), Jiangsu Key Laboratory for Nano Technology, Nanjing University, Nanjing, 210093, China*
[c]*Key Laboratory of Soft Chemistry and Functional Materials (MOE), Nanjing University of Science and Technology, Nanjing 210094, P. R. China. E-mail: yychem@njust.edu.cn*
[d]*Institute of Environmental Energy Materials and Intelligent Devices, School of Metallurgy and Materials Engineering, Chongqing University of Science and Technology, Chongqing 401331, China*
[e]*Yangzhou University, School of Chemical Engineering, Yangzhou 225002, P. R. China*
[f]*School of Science and Engineering, The Chinese University of Hongkong (Shenzhen), Shenzhen, Guangdong 518172, China*
† Electronic supplementary information (ESI) available. See DOI: https://doi.org/10.1039/d2nr01448c

$(A^{n-})_{x/n}{\cdot}yH_2O$, have attracted extensive interest in photocatalysis in recent decades because osf their flexible components and tunable structures.[5,6] Much effort has gone into enhancing the photoinduced CO_2 conversion activity of LDHs through morphological engineering,[7,8] doping engineering,[9] defect engineering,[10–12] semiconductor hybridization,[13,14] cocatalyst incorporation,[15,16] *etc*. Among the above modification strategies, the surface decoration of a photocatalyst with a cocatalyst attracts a high level of attention because it provides surface active sites, reduces the activation energy, facilitates interfacial charge separation and suppresses the reverse reaction.[17–19] For example, Jiang *et al.*[20] prepared a series of Cu_2O-loaded Zn–Cr layered double hydroxides *via* an *in situ* reduction process from Cu–Zn–Cr ternary LDHs, which they applied to the photoreduction of CO_2. The loaded Cu_2O nanoparticles functioned as effective electron traps, greatly promoting charge separation and increasing the number of reactive sites for CO_2 reduction. $0.1Cu_2O$@Zn1.8Cr LDH exhibited a CO yield of up to 6.3 μmol after 24 h of light irradiation. Pt NPs were highly dispersed over exfoliated layered double hydroxide (ex-LDH) *via* electrostatic interaction,[21] and the as-obtained photocatalyst exhibited a high CO evolution rate of 2.64 μmol g^{-1} h^{-1}. However, the CO_2 photoreduction performance of these LDH photocatalytic systems is limited. Therefore, to explore and extend this field, the application of other effective cocatalysts to promote the photocatalytic CO_2 reduction activity of the 2D LDH family of photocatalysts is still required.

As a promising family of 2D layered transition metal carbides/nitrides, MXenes have great potential for application in supercapacitors,[22,23] batteries,[24,25] and electrocatalysis.[26,27] They have the multiple advantages of flexibility of elements,[28] a regular layered structure,[29,30] a highly hydrophilic surface,[31] tunable surface functional groups,[32] good light-harvesting ability,[33] and excellent electrical conductivity.[34,35] Because of their high electron conductivity, MXenes are promising as cocatalysts in photocatalyst systems.[36,37] Additionally, the abundant surface functional groups (–F, –O, –OH) on MXenes benefit their tight coupling with other semiconductors to form heterojunctions,[38,39] thus increasing the migration and separation of carriers.[40–42] For example, Cao *et al.*[43] reported the fabrication of a 2D/2D Ti_3C_2/Bi_2WO_6 heterojunction which showed significant improvement in photocatalytic CO_2 reduction into CH_4 and CH_3OH, with yields of 1.78 and 0.44 μmol h^{-1} g^{-1}. Yang *et al.*[44] prepared an ultrathin 2D/2D Ti_3C_2/g-C_3N_4 heterojunction by direct calcination of a mixture of bulk Ti_3C_2 and urea, and the optimal sample (10TC) exhibited yields of 5.19 and 0.044 μmol h^{-1} g^{-1} for CO and CH_4. However, these product yields are still relatively low. Therefore, the exploration of other highly active heterogeneous photocatalytic systems is of great significance. The attempted combination of an MXene with an unusual LDH for the photoreduction of CO_2 is rare. Therefore, using MXenes to improve the electron separation and migration of LDHs, and therefore to promote the photocatalytic CO_2 reduction activity of LDHs, is the focus of our research.

In this work, we construct a series of ZnCr-LDH/$Ti_3C_2T_x$ composites with different loading amounts of $Ti_3C_2T_x$ using a coprecipitation process. In detail, $Ti_3C_2T_x$ nanosheets were obtained by wet chemical etching Ti_3AlC_2 with subsequent TMAOH (tetramethylammonium hydroxide) intercalation and ultrasonic exfoliation. After cation electrostatic adsorption, the aggregate semi-transparent ZnCr-LDH nanoflakes were grown *in situ* on the surface of the $Ti_3C_2T_x$ nanosheets through coprecipitation to form a tightly coupled Schottky junction. Because of the improved light absorption intensity and reinforced photo-induced carrier separation and migration efficiency, the obtained 2D/2D ZnCr-LDH/$Ti_3C_2T_x$ heterostructures exhibited a significant improvement in photocatalytic CO_2 reduction under simulated solar irradiation. The optimized sample ZCTC25 had the highest photocatalytic CO_2 reduction rates of 122.45 μmol g^{-1} CO and 19.95 μmol g^{-1} CH_4 (after 6 h of irradiation). These values are 2.65 times higher than those for pristine ZnCr-LDH. $Ti_3C_2T_x$ MXene as a support for growing self-assembled ZnCr-LDH nanoflakes to form a Schottky junction is an efficient photocatalyst for enhancing photocatalytic CO_2 reduction.

Experimental

Materials

Zinc nitrate hexahydrate ($Zn(NO_3)_2{\cdot}6H_2O$), chromic nitrate nonahydrate ($Cr(NO_3)_3{\cdot}9H_2O$), sodium hydroxide (NaOH), ammonium carbonate (Na_2CO_3), hydrofluoric acid (HF, content ≥40.0%), tetramethylammonium hydroxide (TMAOH) and Ti_3AlC_2 powder were purchased from Forsman Scientific (Beijing) Co., Ltd. All of the above reagents were of A. R. grade and used without further purification. Deionized (DI) water was used for all experiments.

Synthesis of $Ti_3C_2T_x$ MXene nanosheets

All reagents used were of analytical grade and were used as received without further purification. $Ti_3C_2T_x$ MXene was synthesized *via* selective etching of Al from Ti_3AlC_2 using concentrated hydrofluoric acid solution. Specifically, 1 g of Ti_3AlC_2 powder was slowly added to 20 mL of HF to avoid overheating under continuous stirring at room temperature for 18 h. The mixture was then centrifuged and washed repeatedly with deionized (DI) water to reach pH ~7. The black multilayered $Ti_3C_2T_x$ (~0.6–0.9 g) was obtained after freeze-drying. To obtain $Ti_3C_2T_x$ MXene nanosheets, 0.5 g of $Ti_3C_2T_x$ MXene powder was wetted with 5 mL of tetramethylammonium hydroxide (TMAOH) as an intercalator and the mixture was then diluted with 10 mL of DI water. After stirring at room temperature for 24 h, the basic $Ti_3C_2T_x$ MXene solution was brought to a neutral pH by washing in DI water four times using centrifugation (2 min per cycle at 8000 rpm). To delaminate, the sediment was then re-dispersed in 50 mL of DI water and ultrasonicated under Ar protection for 30 min. The suspension was centrifuged at 3500 rpm for 20 min to obtain the

few-layered $Ti_3C_2T_x$ MXene supernatant and the unexfoliated solid apart. Finally, the few-layered $Ti_3C_2T_x$ MXene supernatant was collected after three solid ultrasonication and centrifugation cycles, and the concentration was measured to be 1.2 mg mL^{-1}. The obtained supernatant was stored at a low temperature (~5 °C) for further use.

Synthesis of ZnCr-LDH/$Ti_3C_2T_x$ hybrids

Solution A was prepared by dissolving 5 mmol of $Zn(NO_3)_2{\cdot}6H_2O$ and 2.5 mmol of $Cr(NO_3)_3{\cdot}9H_2O$ in 30 mL of DI water, then adding various amounts of $Ti_3C_2T_x$ MXene supernatant (containing 5 mg, 25 mg and 50 mg $Ti_3C_2T_x$ MXene, respectively). The solution was ultrasonicated to obtain a homogeneous solution. Solution B was prepared by dissolving 15 mmol of NaOH and 12.5 mmol of Na_2CO_3 in 40 ml of DI water. Solution B was added dropwise into solution A under constant stirring. The resulting slurry was heated at 60 °C in an oil bath for 24 h. The precipitate obtained was collected using centrifugation, washed several times with DI water and then freeze-dried overnight. The as-prepared samples were labeled ZCTC5, ZCTC25 and ZCTC50. The actual contents of $Ti_3C_2T_x$ MXene in ZCTC5, ZCTC25 and ZCTC50 were calculated to be 0.10%, 0.51% and 0.99%, respectively, measured by inductively coupled plasma-optical emission spectrometry (ICP-OES, Table S1†).

Synthesis of ZnCr-LDH

The procedure was similar to the synthesis steps used for the ZnCr-LDH/$Ti_3C_2T_x$ hybrids, without the addition of $Ti_3C_2T_x$ nanosheets.

Characterization

The XRD patterns of the obtained samples were recorded using an X-ray diffractometer (XRD, TD-3500), using Cu Kα radiation (α = 1.542 Å) at an operating voltage of 30 kV and a current of 20 mA, with a scanning rate of 6° min^{-1}. The morphology was characterized using field emission scanning electron microscopy (FESEM, ZEISS GeminiSEM 500). Transmission electron microscopy (TEM) and fine resolution transmission electron microscopy (HRTEM) images were recorded using an FEI TECNAI F20 apparatus. X-ray photoelectron spectroscopy (XPS) was carried out using a ULVAC PHI5000 VersaProbe and all binding energies were calibrated using the adventitious C 1s peak at 284.8 eV to inspect the chemical state. UV-visible diffuse reflectance spectra were recorded using a UV-vis spectrophotometer (UV-2550, Shimadzu), and then switched to the absorption spectra on the basis of the Kubelka–Munk relationship. $BaSO_4$ was used as the standard. The N_2 adsorption–desorption and CO_2 adsorption were carried out on TriStar 3000. *In situ* Fourier transform infrared (*in situ* FTIR) spectroscopy was analyzed using a Nicolet NEXUS870 (USA) spectrometer. The inductively coupled plasma-optical emission spectrometry (ICP-OES) was performed on Thermo Fisher iCAP PRO.

Photocatalytic CO_2 reduction

Typically, 30 mg samples were uniformly dispersed on the glass reactor with an area of 4.2 cm^2. A 300 W xenon arc lamp was used as the light source for the photocatalytic reaction. The light intensity is 95.1 mW cm^2 at the wavelength of 385 nm. The volume of the reaction system was approximately 460 mL. Before the irradiation, high purity CO_2 was bubbled into the reaction jar for 20 min to reach ambient pressure and sealed. 0.4 mL of deionized water was injected into the reaction system as a reducer. The photocatalysts stood for some time in the CO_2/H_2O atmosphere to ensure that the adsorption of gas molecules was complete. During the irradiation, 1 mL of gas was extracted from the reaction system per hour and injected into the gas chromatographic column for CO and CH_4 concentration analysis using a gas chromatograph (GC-2014C, Shimadzu Corp., Japan). And the O_2 was detected with the column TCD equipped on it.

Photoelectrochemical performance measurements

Photoelectrochemical measurements were made using a CHI-660E workstation (Shanghai Chen Hua Co., Ltd) with a conventional three-electrode cell, which consisted of a counter electrode (Pt foil), a reference electrode (Ag/AgCl), and a working electrode (FTO glass). 0.5 M Na_2SO_4 solution was used as the electrolyte. The working electrode was prepared as follows: 30 mg of the as-prepared sample was dispersed in 30 mL of acetone with 15 mg of iodine. This suspension was evenly coated on the FTO glass within a 1 cm^2 area using an electrophoresis method and then dried at room temperature.

Results and discussion

Fig. 1 illustrates the whole synthetic process for producing the ZnCr-LDH/$Ti_3C_2T_x$ (ZCTC) composites. The process includes four stages: selective etching, intercalation and exfoliation, electrostatic adsorption and *in situ* coprecipitation. In detail, the aluminum in ternary MAX (Ti_3AlC_2) was selectively etched using HF to achieve bulk $Ti_3C_2T_x$ with a multilayer structure. Through TMAOH intercalation overnight and ultrasonic exfoliation, the negatively charged delaminated few-layer $Ti_3C_2T_x$ nanosheets were uniformly dispersed in an aqueous solution. Next, positively charged Zn^{2+} and Cr^{3+} ions were electro-

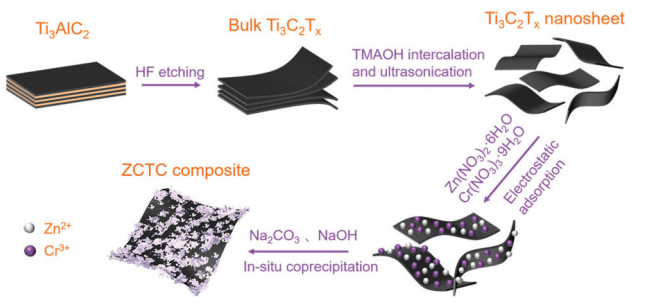

Fig. 1 Schematic illustration of the synthesis of the ZCTC composite.

statically adsorbed on the $Ti_3C_2T_x$ nanosheets. Alkali was slowly dropped in and the mixed solution stirred constantly to complete the *in situ* coprecipitation process. Finally, small LDH nanoflakes were grown in aggregate on the flat $Ti_3C_2T_x$ nanosheets to form the heterostructure.

The crystal structure and phase characteristics of the as-prepared samples were studied using X-ray diffraction (XRD) analysis. As shown in Fig. S1,† the MAX phase exhibits intense peaks, which can be assigned to Ti_3AlC_2 according to previous reports.[45] After etching treatment using HF, the (104) diffraction peak located at 39° (2θ) was not observed, indicating that the Al in Ti_3AlC_2 was removed. Additionally, the (002) and (004) peaks were shifted towards lower diffraction angles of 8.8° and 17.8°, indicating a broader plane spacing. This indicates that $Ti_3C_2T_x$ MXene was successfully synthesized. Additionally, compared with Ti_3AlC_2, the peak intensities of $Ti_3C_2T_x$ were weak, which can be ascribed to the thinner layered structure of $Ti_3C_2T_x$.[43,46] Meanwhile, the 'black' colloidal solution of the $Ti_3C_2T_x$ nanosheets after ultrasonication exhibit a typical Tyndall effect (Fig. S2†), suggesting the formation of a homogeneous dispersion of $Ti_3C_2T_x$ nanosheets. As shown in Fig. 2a, the XRD peaks of the composites located at 11.7°, 23.4°, 34.0°, 38.9°, 59.3° and 60.5° can be ascribed to the (003), (006), (012), (015), (110) and (113) planes of a rhombohedral hydrotalcite-like ZnCr-LDH structure (ICDD card no. 052-0010) without co-crystallization of any impurity phases.[47] Upon increasing the amount of $Ti_3C_2T_x$ MXene, no characteristic peak (002) of $Ti_3C_2T_x$ was observed for the ZnCr-LDH/$Ti_3C_2T_x$ nanomaterials. This is because of the relatively low additive amount and the dispersion of the MXene layers.[48,49]

Fig. 2b shows the FTIR spectra of the samples. As reported previously,[50] there are no clear peaks in the $Ti_3C_2T_x$ spectrum, and the overall infrared absorption of the composite ZCTC is similar to that of ZnCr-LDH, suggesting that the signals in ZCTC are from ZnCr-LDH. Specifically, the peak at approximately 3400 cm^{-1} originates from the stretching vibration of the hydroxyl radical in the LDH host layer and interlayer water molecules.[20] The peak at approximately 1630 cm^{-1} can be attributed to the bending vibration of lattice water.[20] The peaks at approximately 1360 and 780 cm^{-1} are assigned to the anti-symmetric stretching mode and bending vibration of CO_3^{2-}, respectively.[46] As shown in Fig. 2c, the Raman peaks at approximately 1380 and 1560 cm^{-1} correspond to the characteristic D and G bands of carbon,[48] respectively, which are both detected in $Ti_3C_2T_x$ and ZCTC25. In addition, the Raman peak at 1061 cm^{-1} for ZnCr-LDH is assigned to in-plane OH bending vibrations.[51] This peak distinctly shifts lower to 992 cm^{-1} for ZCTC25, suggesting an interface interaction between ZnCr-LDH and $Ti_3C_2T_x$ MXene.

To examine the morphology and nanostructure composition of the as-prepared samples, field emission scanning electron microscopy (FESEM) and transmission electron microscopy (TEM) were employed. Few-layer and single-layer $Ti_3C_2T_x$ nanosheets were obtained by etching Ti_3AlC_2 into $Ti_3C_2T_x$, with subsequent ultrasonic exfoliation treatment. As shown in Fig. 3a and S3a,† bulk $Ti_3C_2T_x$ MXene was observed after the Al layer was eliminated from Ti_3AlC_2 by the HF etching process, exhibiting a loose, accordion-like structure. Fig. 3b and S3b† show the delaminated thinner 2D $Ti_3C_2T_x$ nanosheets with a typical 2D layered structure of which the lateral size is around 300–400 nm. This indicates the successful exfoliation of bulk $Ti_3C_2T_x$. Pure ZnCr-LDH (Fig. 3c and S4a†) exists in the form of solid agglomerates consisting of numerous irregular 2D nanoflakes. This can also be demonstrated by TEM—Fig. 3d and S4b† show a consistent microstructure with self-assembled translucent nanoflakes matching the SEM image of pure ZnCr-LDH. It can be seen from Fig. 3e, f and Fig. S4c, d† that the ZnCr-LDH nanoflakes grow *in situ* on the surface of the $Ti_3C_2T_x$ MXene nanosheets. Because of the terminated functional group (T = –F, –OH, –O), $Ti_3C_2T_x$ MXene is negatively charged. Therefore, the electrostatic interaction between $Ti_3C_2T_x$ MXene nanosheets and Zn^{2+}, Cr^{3+} could explain the growth of ZnCr-LDH onto the $Ti_3C_2T_x$ MXene nanosheets. Fig. 3f shows that the ZCTC25 exhibits distinctly different areas of morphology, which are labeled as ZnCr-LDH and $Ti_3C_2T_x$ MXene. In the magnified region (Fig. 3g), we also observed the coexistence of two interplanar

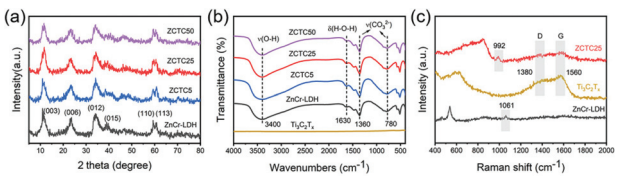

Fig. 2 (a) XRD patterns of pristine ZnCr-LDH and composites with different masses of $Ti_3C_2T_x$ (5 mg, 25 mg, 50 mg). (b) FTIR spectra of $Ti_3C_2T_x$, ZnCr-LDH and composites ZCTC with different $Ti_3C_2T_x$ loading amounts. (c) Raman spectra of ZnCr-LDH, $Ti_3C_2T_x$ and ZCTC25.

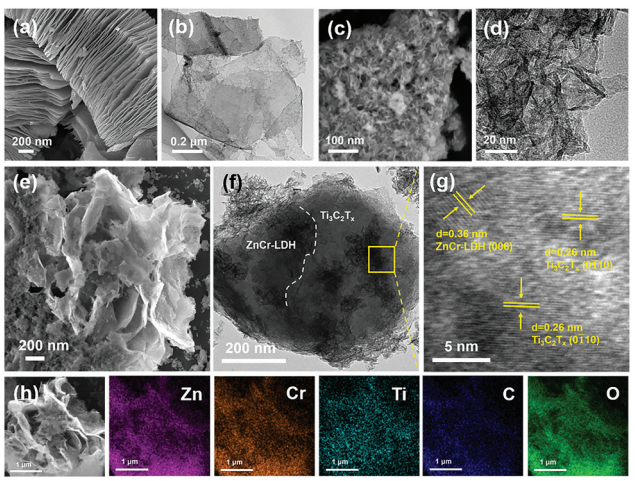

Fig. 3 (a) SEM image of multi-layered $Ti_3C_2T_x$ nanosheets. (b) TEM image of exfoliated few-layered $Ti_3C_2T_x$ nanosheets. (c and d) SEM and TEM images of collectively-grown translucent nanoflakes of pristine ZnCr-LDH, respectively. (e and f) SEM and TEM images of ZCTC25, respectively. (g) HRTEM image of ZCTC25. (h) SEM elemental mapping images of ZCTC25.

spacings, 0.26 nm and 0.36 nm, corresponding to the $Ti_3C_2T_x$ (0 $\bar{1}$ 10) plane and the ZnCr-LDH (006) plane, respectively. This indicates the close integration of the two materials and the successful formation of a heterostructure interface between the ZnCr-LDH and $Ti_3C_2T_x$ MXene nanosheets, which facilitates the separation and transfer of photoexcited carriers. As shown in Fig. 3h, the uniform distribution of Zn, Cr, Ti, C and O in the selected area observed using elemental mapping of FESEM further confirms the successful synthesis of the ZCTC25 heterostructure.

To investigate the surface chemical composition and state of the as-prepared samples, X-ray photoelectron spectroscopy (XPS) analysis was conducted. All the binding energies were calibrated using the C 1s peak located at 284.8 eV, which was assigned to adventitious carbon (C–C). As shown in the XPS survey spectra (Fig. 4a), Ti, C, O and F were observed in $Ti_3C_2T_x$ MXene. Furthermore, Zn, Cr, C and O were observed in both ZnCr-LDH and ZCTC25. For ZCTC25, no F or Ti was detected, and the absence of the F 1s peak located at 684.8 eV was further confirmed by high-resolution spectra (Fig. S5a†). This indicated that *F* was fully removed after the TMAOH intercalation and co-precipitation process. Although Ti does not appear in the XPS survey spectra, the high-resolution spectra of ZCTC25 Ti 2p (Fig. S5b†) shows its existence in the ZnCr-LDH/$Ti_3C_2T_x$ composites, with two characteristic peaks at 458.5 and 461.7 eV, which can be assigned to the Ti–O and Ti–C bonds, respectively.[43] As shown in the high-resolution XPS spectra of Ti 2p in $Ti_3C_2T_x$ (Fig. S6†), the binding energies at 454.5, 455.3 (460.8) and 456.9 (462.3) eV correspond to Ti–C, Ti^{2+} and Ti^{3+}, respectively. Fig. 4b shows the high-resolution C 1s spectra of $Ti_3C_2T_x$ and ZCTC25. $Ti_3C_2T_x$ shows three characteristic peaks at 281.6, 286.1 and 288.8 eV, which are assigned to the C–Ti, C–O and C–F bonds, respectively.[43] For ZCTC25, the binding energies of C 1s at 286.3 and 288.7 eV are assigned to the C–O and O–C=O bonds, respectively. C–Ti cannot be detected in ZCTC25 because of the small amount of $Ti_3C_2T_x$ MXene nanosheets. The C 1s peaks shown in Fig. S7† at binding energies of 284.8, 286.3 and 288.9 eV suggest the presence of a carbonate anion in the structure of the ZnCr-LDH. As shown in Fig. 4c and d, in ZnCr-LDH and ZCTC25, Zn 2p and Cr 2p are both deconvoluted into two peaks. The absorption peaks at 1021.8 and 1044.8 eV for ZnCr-LDH are assigned to Zn $2p_{3/2}$ and Zn $2p_{1/2}$, respectively, with a doublet separation of 23.0 eV. This indicates the existence of Zn^{2+}. The absorption peaks at 577.4 and 586.6 eV for ZnCr-LDH are assigned to Cr $2p_{3/2}$ and Cr $2p_{1/2}$, respectively, with a doublet separation of 9.2 eV. This is consistent with the Cr^{3+} valence state. The binding energies of Zn $2p_{3/2}$, Zn $2p_{1/2}$, Cr $2p_{3/2}$ and Cr $2p_{1/2}$ in ZCTC25 are 1022.5, 1045.5, 578.1 and 587.3 eV, showing a positive chemical shift of 0.7 eV compared to ZnCr-LDH. This suggests that electrons are transferred from ZnCr-LDH to $Ti_3C_2T_x$ MXene, building up a strong interface interaction between ZnCr-LDH and the $Ti_3C_2T_x$ MXene nanosheets. Additionally, a broader full width at half-maximum is present in the Zn 2p spectrum of ZCTC25, because of the enhanced disorder after the loading of $Ti_3C_2T_x$ MXene nanosheets.

The optical absorption properties of all as-prepared samples were measured using ultraviolet-visible diffuse reflectance spectroscopy (UV-vis DRS). As shown in Fig. 5a, ZnCr-LDH exhibits two absorption peaks in the visible region. The one at approximately 410 nm was assigned to the ligand-to-metal charge-transfer effect from O_{2p} to Cr-$3dt_{2g}$, and the other at approximately 570 nm was assigned to Cr-$3dt_{2g}$ → Cr-$3de_g$ (d–d transition) of Cr^{3+}.[52] Upon increasing the loading content of the $Ti_3C_2T_x$ MXene nanosheets, the light absorption intensity of all the composites is increasingly promoted in a

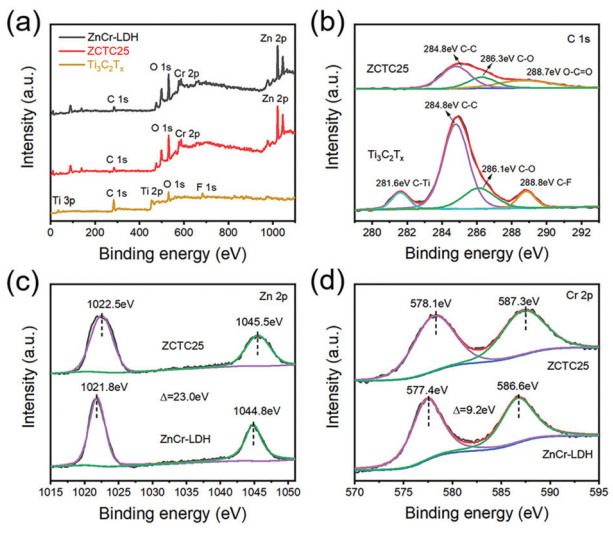

Fig. 4 (a) XPS survey of ZnCr-LDH, ZCTC25 and $Ti_3C_2T_x$. (b) High-resolution XPS C 1s spectra of ZCTC25 and $Ti_3C_2T_x$. (c) High-resolution XPS Zn 2p spectra of ZCTC25 and ZnCr-LDH. (d) High-resolution XPS Cr 2p spectra of ZCTC25 and ZnCr-LDH.

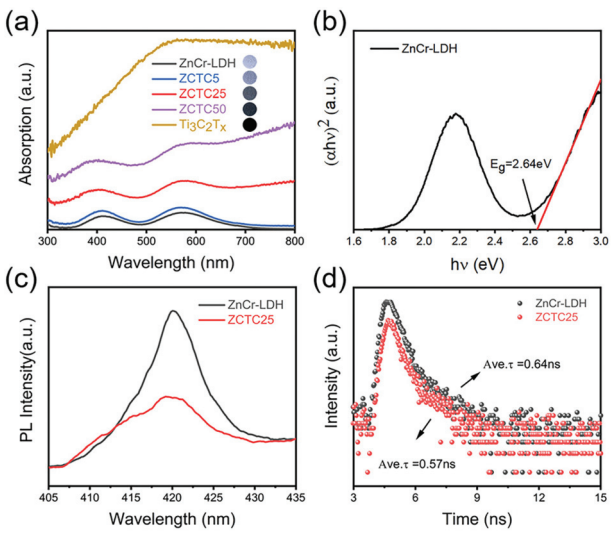

Fig. 5 (a) UV-vis DRS of ZnCr-LDH, $Ti_3C_2T_x$, ZCTC5, ZCTC25 and ZCTC50. (b) Tauc energy gap plot of ZnCr-LDH. (c) Steady-state photoluminescence spectra of ZnCr-LDH and ZCTC25. (d) Time-resolved transient photoluminescence decay spectra of ZnCr-LDH and ZCTC25.

wide spectral range of 300–800 nm. The increase in light absorption intensity is caused by the full-spectrum absorption properties of $Ti_3C_2T_x$ MXene. This reflects the metallic nature of $Ti_3C_2T_x$ MXene. The band-gap energy (E_g) of the pristine ZnCr-LDH is estimated to be 2.64 eV based on the Tauc plot (Fig. 5b). Steady-state photoluminescence and time-resolved transient photoluminescence decay spectra were recorded using an excitation wavelength of 405 nm, and are shown in Fig. 5c and d. The composite ZCTC25 exhibits a decreased photoluminescence intensity, indicating suppressed electron–hole recombination compared to pristine ZnCr-LDH. In addition, the average photoluminescence lifetime was reduced from 0.64 to 0.57 ns upon the introduction of $Ti_3C_2T_x$ into ZnCr-LDH, indicating the presence of a non-radiation decay pathway,[43] which is caused by electron transfer from ZnCr-LDH to $Ti_3C_2T_x$.

Photocatalytic CO_2 reduction was performed in a glass reactor filled with high purity CO_2 gas (>99.995%) under simulated solar irradiation, and a small amount of water was added. As shown in Fig. 6a and b, carbon monoxide (CO) and methane (CH_4) were both produced under reduction conditions and product growth was proportional to time. As shown in Fig. 6c, when the $Ti_3C_2T_x$ MXene was introduced into ZnCr-LDH to form the nanohybrid, the product yields of CO and CH_4 both increased until the loading capacity of $Ti_3C_2T_x$ MXene exceeded the optimal value. The ZCTC25 composite exhibited the highest photocatalytic CO_2 reduction activity with CO and CH_4 yields of 122.45 and 19.95 μmol g^{-1}, respectively (after 6 h of irradiation), which is around 2.65 times higher than the values for pristine ZnCr-LDH (46.34 μmol g^{-1} CO and 7.48 μmol g^{-1} CH_4). The CO_2 reduction performance of ZCTC50 declines mainly because excess $Ti_3C_2T_x$ MXene can hinder the metal active sites. Although CO and CH_4 are both photocatalytic CO_2 reduction products of the as-prepared samples, the composites present higher selectivity toward CO gas. For ZCTC25, the CO product selectivity was calculated to be 86% $\left(\text{selectivity} = \frac{N_{CO}}{N_{(CH_4+CO)}} \times 100\%\right)$ in 6 h. The photo-generated holes in the VB of ZnCr-LDH oxidize H_2O to produce hydrogen ions by the reaction of $H_2O \rightarrow 1/2O_2 + 2H^+ + 2e^-$. CO is formed by reacting with two protons and two electrons ($CO_2 + 2H^+ + 2e^- \rightarrow CO + H_2O$), and CH_4 formation through accepting eight electrons and eight protons ($CO_2 + 8H^+ + 8e^- \rightarrow CH_4 + H_2O$). And the competitive reaction of water splitting also occurred ($H_2O \rightarrow H_2 + O_2$), because the H_2 and O_2 were observed after irradiation because of the competitive reaction of water splitting, as shown in Fig. S9 and Fig. S10.† While the performance of physically mixed ZCTC composite without forming the Schottky junction is lower than that of ZCTC25 synthesized through *in situ* coprecipitation method (Fig. S13a and b†). Therefore, after a tight contact was formed between ZnCr-LDH and $Ti_3C_2T_x$ MXene, the separation and shifting efficiency of the interface charge was greatly enhanced, leading to efficient electron transfer from ZnCr-LDH to $Ti_3C_2T_x$, which increased the photocatalytic CO_2 reduction ability.

When the photocatalyst is under dark conditions or an Ar atmosphere, there are no conversion products, as shown in Fig. S11.† To determine the carbon source of the reaction products, gas chromatography-mass spectrometry (GC-MS) was used to detect CO labeled with ^{13}C.[55] As shown in Fig. 6d, the ^{13}CO peak appears at a retention time of 1.225 min consistent with the peak position in the mass spectra when using $^{13}CO_2$ as the carbon source. The base peak at m/z = 29 in the mass spectrum indicates that the relative atomic mass of carbon in the CO product is 13 (Fig. 6d inset image). Therefore, it is clear that the photocatalytic reaction products originate from CO_2 conversion.

The N_2 adsorption and desorption were carried out for the pristine ZnCr-LDH and ZCTC25 samples to determine the porosity, specific surface area and pore size distribution. As shown in Fig. S12a,† both samples exhibit the Type IV isotherm with a hysteresis loop, which is given by mesoporous adsorbents. The hysteresis loop is further classified to be the Type H3 loop because the adsorption branch resembles a Type II isotherm and the lower limit of the desorption branch is normally located at the cavitation-induced p/p_0. Loop of Type H3 is given by non-rigid aggregates of plate-like particles.[53,54] The surface area of ZnCr-LDH and ZCTC25 samples are calculated to be 59.64 and 42.28 m^2 g^{-1}, respectively, using the Brunauer–Emmett–Teller (BET) model. Shown by the pore size distribution (inset image), the range is from 17 to 1300 nm while the most probable pore size is 36 nm, which is further verifying the mesoporous nature of the materials. The CO_2 adsorption ability of ZCTC25 with 24.16 cm^3 g^{-1} is slightly weaker than pristine ZnCr-LDH with 24.93 cm^3 g^{-1}, as shown in Fig. S12b,† which can be relative to the smaller specific surface area of ZCTC25. However, the higher photocatalytic CO_2 reduction performance of ZCTC25 indicates that its surface area and CO_2 affinity are not the main factors impacting photoactivity of ZnCr-LDH/$Ti_3C_2T_x$ composites.

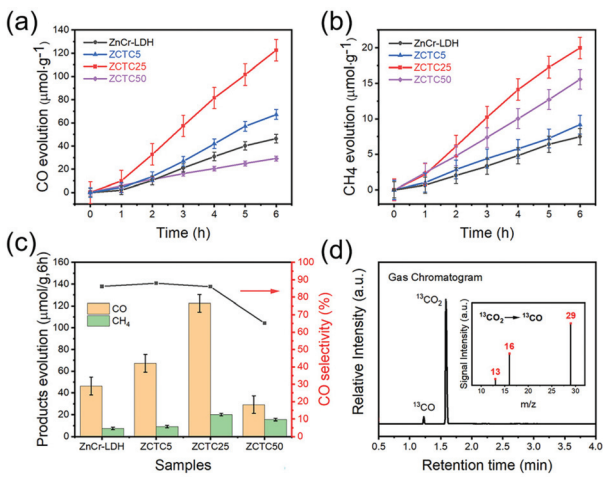

Fig. 6 (a and b) Time plots of CO and CH_4 evolution for ZnCr-LDH, ZCTC5, ZCTC25 and ZCTC50 under irradiation for 6 h. (c) Photocatalytic CO_2 reduction performance and product selectivity for CO molecules for ZnCr-LDH, ZCTC5, ZCTC25 and ZCTC50. (d) GC-MS spectrum for ZCTC25 (main image) and m/z analysis of generated CO with $^{13}CO_2$ as the carbon source (inset image).

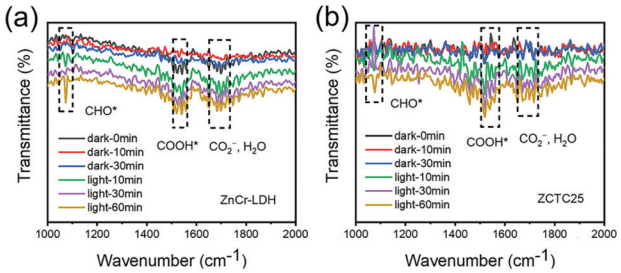

Fig. 7 (a) *In situ* FTIR spectra of pristine ZnCr-LDH under dark and light irradiation for a different time. (b) *In situ* FTIR spectra of composite ZCTC25 under dark and light irradiation for a different time.

In situ Fourier transform infrared spectroscopy (*in situ* FTIR) measurement was conducted to detect the intermediates of CO_2 photoreduction over pristine ZnCr-LDH and composite ZCTC25 (Fig. 7a and b). It shows that the characteristic peak at around 1550 cm^{-1} of both samples can be ascribed to the COOH* group, which is the crucial intermediate for reducing CO_2 to CO.[56] The absorption peak at approximately 1072 cm^{-1} is caused by the CHO* group resulting from successive protonation of CO_2 molecules, which is the intermediate for reducing CO_2 to CH_4.[57] At the same time, the band at around 1680 cm^{-1} is attributed to the asymmetric vibration of bicarbonate (CO_2^-) and adsorbed H_2O.[58]

Photoelectrochemical tests were used to determine the charge transfer ability. ZCTC25 exhibits a smaller arc radius than the pristine ZnCr-LDH in the electrochemistry impedance spectroscopy (EIS) Nyquist plot, as shown in Fig. 8a, indicating its lower electrical resistance. Therefore, ZCTC25possesses high-speed channels for fast transfer and efficient separation of photoexcited charges. The decreased electrical resistance of ZCTC25 can presumably be ascribed to the high electrical conductivity and superb charge migration of MXene. Additionally, the transient photocurrent spectra (Fig. 8b) show that ZCTC25 has a higher photocurrent density than pristine ZnCr-LDH, indicating enhanced charge transfer kinetics in ZCTC25. The increased photocurrent density of ZCTC25 maybe because of the ability of MXene to improve the light absorption and enhance the charge separation.[49] These results prove that the ZCTC25 heterostructure inhibits electron–hole recombination and improves the photoexcited carrier separation.

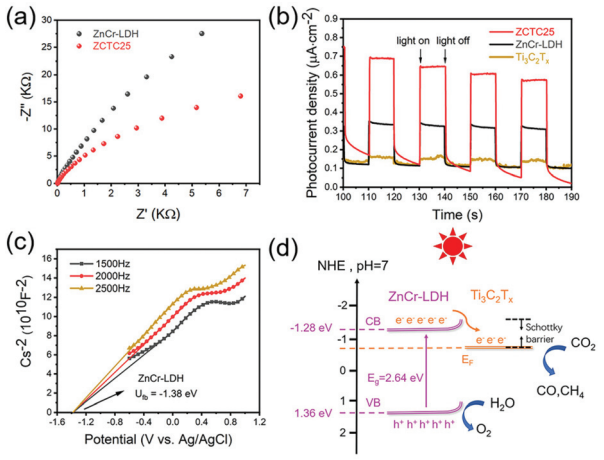

Fig. 8 (a) EIS Nyquist plot and (b) transient photocurrent spectra of ZnCr-LDH, Ti_3C_2Tx and ZCTC25. (c) Mott–Schottky plots of ZnCr-LDH at three different frequencies. (d) Schematic diagram of charge transfer over the ZCTC composite under simulated solar irradiation.

It can be seen that the Mott–Schottky (MS) curves possess a positive slope at different frequencies (from 1500 to 2500 Hz), indicating that ZnCr-LDH is a typical n-type semiconductor (Fig. 8c). The Fermi level (E_F) is nearly equal to the flat-band potential (U_{fb}), which is approximately −1.38 eV (*vs.* Ag/AgCl, pH = 7) derived from the intercept of the tangent of the MS curves on the *x*-axis. The E_F *vs.* Ag/AgCl, pH = 7, is approximately 0.2 eV more negative than the E_F *vs.* NHE, pH = 7. Therefore, the E_F *vs.* NHE, pH = 7, is calculated to be −1.18 eV. In general, the conduction band (CB) of the n-type semiconductor is approximately 0.10 eV more negative than the E_F.[59,60] Therefore the CB value (E_{CB}) of ZnCr-LDH is estimated to be −1.28 eV (*vs.* NHE, pH = 7). On account of the E_g of ZnCr-LDH being 2.64 eV, the valence band value (E_{VB}) is calculated to be 1.36 eV (*vs.* NHE). This is consistent with the XPS-VB value, which was determined to be 1.35 eV from the XPS valence spectrum (Fig. S8†). According to previous reports, the E_F values of $Ti_3C_2T_x$ with terminal –F, and $Ti_3C_2T_x$ with terminal –O, are calculated to be 0.18 eV and 0.71 eV, respectively (*vs.* NHE, pH = 7).[43] These values are much lower than the conduction band position of ZnCr-LDH, and therefore the photoexcited electrons tend to transfer from ZnCr-LDH to $Ti_3C_2T_x$ across the heterojunction interface.

Based on the results discussed above, a photocatalytic process for the ZnCr-LDH/$Ti_3C_2T_x$ heterostructure is proposed. The Fermi level of ZnCr-LDH is higher than that of $Ti_3C_2T_x$ before contact, as indicated by the above MS measurements. Therefore, the difference between the Fermi levels for ZnCr-LDH and $Ti_3C_2T_x$ drives the electron migration from ZnCr-LDH to $Ti_3C_2T_x$ after their contact to equilibrate the E_F between the two materials. In the equilibrium process, the energy band of ZnCr-LDH (an n-type semiconductor) will bend upwards to produce a Schottky barrier, as shown in Fig. 8d. Under simulated solar irradiation, the photo-induced electrons are excited and leap from the CB to the VB of ZnCr-LDH, and holes are left in the VB. Then, the electrons migrate along the Schottky junction to $Ti_3C_2T_x$, achieving efficient electron separation. Their backflow is prevented by the Schottky barrier. After that, the electrons accumulated at the E_F of $Ti_3C_2T_x$ react with adsorbed CO_2 molecules and reduce them to CO and CH_4 gas. Meanwhile, the holes gathered on the VB of ZnCr-LDH are consumed by sacrificial H_2O. In brief, the enhanced photocatalytic CO_2 reduction performance is a result of the increased photogenerated electron separation and migration along with the heterojunction interface between ZnCr-LDH and $Ti_3C_2T_x$ MXene.

Conclusions

In summary, a novel 2D/2D ZnCr-LDH/$Ti_3C_2T_x$ Schottky heterojunction is synthesized using an *in situ* coprecipitation

method. ZnCr-LDH nanoflakes collectively grow on the surface of $Ti_3C_2T_x$ MXene nanosheets. The heterojunction of ZnCr-LDH/$Ti_3C_2T_x$ exhibits significantly improved photocatalytic CO_2 reduction under simulated solar irradiation. The optimized sample ZCTC25 has the highest photocatalytic CO_2 reduction rates of 122.45 μmol g^{-1} CO and 19.95 μmol g^{-1} CH_4 (after 6 h of irradiation). These values are approximately 2.65 times higher than those for pristine ZnCr-LDH, which are 46.34 μmol g^{-1} CO and 7.48 μmol g^{-1} CH_4. The product selectivity towards CO gas is 86%. These results can be attributed to the improved light absorption, the promoted charge separation and the migration of the prepared heterojunction after decoration with $Ti_3C_2T_x$ MXene as a cocatalyst. This work further improves the photocatalytic CO_2 reduction performance of ZnCr-LDH by using MXene as a cocatalyst and enriches the application of an unusual type of layered double hydroxides in the photoreduction of CO_2.

Author contributions

B. Zhou contributed to the experiment, investigation, analysis and writing – original draft. Z. Liu contributed to the experiment. Y. Yang contributed to the methodology, writing – review & editing, and supervision. N. Wu contributed to SEM results. Y. Yan contributed to Raman measurement. W. Zhao contributed to XRD implementation. H. He, J. Du and Y. Zhang contributed to the manuscript preparation. Y. Zhou contributed to the conceptualization, methodology, writing – review & editing, funding acquisition and supervision. Z. Zou contributed to funding acquisition and supervision.

Conflicts of interest

There are no conflicts to declare.

Acknowledgements

The authors wish to acknowledge the support of the National Key R & D Program of China (2018YFE0208500), NSF of China (21972065), the Hefei National Laboratory for Physical Sciences at the Microscale (KF2020006), NFS of Jiangsu Province (No. BK20220006), the Program for Guangdong Introducing Innovative and Enterpreneurial Team (2019ZL08L101) and the University Development Fund (UDF01001159).

Notes and references

1 F. Xu, K. Meng, B. Cheng, S. Wang, J. Xu and J. Yu, *Nat. Commun.*, 2020, **11**, 4613.
2 N.-N. Vu, S. Kaliaguine and T.-O. Do, *Adv. Funct. Mater.*, 2019, **29**, 1901825.
3 J. Di, J. Xiong, H. Li and Z. Liu, *Adv. Mater.*, 2018, **30**, 1704548.
4 X. Sun, H. Huang, Q. Zhao, T. Ma and L. Wang, *Adv. Funct. Mater.*, 2020, **30**, 1910005.
5 X. Bian, S. Zhang, Y. Zhao, R. Shi and T. Zhang, *InfoMat*, 2021, **3**, 719.
6 Y. Zhao, X. Jia, G. I. N. Waterhouse, L.-Z. Wu, C.-H. Tung, D. O'Hare and T. Zhang, *Adv. Energy Mater.*, 2016, **6**, 1501974.
7 J. An, T. Shen, W. Chang, Y. Zhao, B. Qi and Y.-F. Song, *Inorg. Chem. Front.*, 2021, **8**, 996.
8 W.-K. Jo, Y.-G. Kim and S. Tonda, *J. Hazard. Mater.*, 2018, **357**, 19.
9 W.-K. Jo, S. Kumar and S. Tonda, *Composites, Part B*, 2019, **176**, 107212.
10 Y. Zhao, G. Chen, T. Bian, C. Zhou, G. I. N. Waterhouse, L.-Z. Wu, C.-H. Tung, L. J. Smith, D. O'Hare and T. Zhang, *Adv. Mater.*, 2015, **27**, 7824.
11 L. Tan, S.-M. Xu, Z. Wang, Y. Xu, X. Wang, X. Hao, S. Bai, C. Ning, Y. Wang, W. Zhang, Y. K. Jo, S.-J. Hwang, X. Cao, X. Zheng, H. Yan, Y. Zhao and H. Duan, *Angew. Chem., Int. Ed.*, 2019, **58**, 11860.
12 K. Wang, C. Miao, Y. Liu, L. Cai, W. Jones, J. Fan, D. Li and J. Feng, *Appl. Catal., B*, 2020, **270**, 118878.
13 S. Tonda, S. Kumar, M. Bhardwaj, P. Yadav and S. Ogale, *ACS Appl. Mater. Interfaces*, 2018, **10**, 2667.
14 Y. Yang, J. Wu, T. Xiao, Z. Tang, J. Shen, H. Li, Y. Zhou and Z. Zou, *Appl. Catal., B*, 2019, **255**, 117771.
15 S. Zhao, D. Pan, Q. Liang, M. Zhou, C. Yao, S. Xu and Z. Li, *J. Phys. Chem. C*, 2021, **125**, 10207.
16 W. Chen, B. Han, Y. Xie, S. Liang, H. Deng and Z. Lin, *Chem. Eng. J.*, 2020, **391**, 123519.
17 J. Ran, J. Zhang, J. Yu, M. Jaroniec and S. Z. Qiao, *Chem. Soc. Rev.*, 2014, **43**, 7787.
18 B. Qiu, M. Du, Y. Ma, Q. Zhu, M. Xing and J. Zhang, *Energy Environ. Sci.*, 2021, **14**, 5260.
19 G. Zhao and X. Xu, *Nanoscale*, 2021, **13**, 10649.
20 H. Jiang, K. Katsumata, J. Hong, A. Yamaguchi, K. Nakata, C. Terashima, N. Matsushita, M. Miyauchi and A. Fujishima, *Appl. Catal., B*, 2018, **224**, 783.
21 J. Xu, X. Liu, Z. Zhou, L. Deng, L. Liu and M. Xu, *Energy Fuels*, 2021, **35**, 10820.
22 M. Hu, H. Zhang, T. Hu, B. Fan, X. Wang and Z. Li, *Chem. Soc. Rev.*, 2020, **49**, 6666.
23 Y. Zhou, K. Maleski, B. Anasori, J. O. Thostenson, Y. Pang, Y. Feng, K. Zeng, C. B. Parker, S. Zauscher, Y. Gogotsi, J. T. Glass and C. Cao, *ACS Nano*, 2020, **14**, 3576.
24 C. (J.) Zhang, L. Cui, S. Abdolhosseinzadeh and J. Heier, *InfoMat*, 2020, **2**, 613.
25 M. Shi, B. Wang, Y. Shen, J. Jiang, W. Zhu, Y. Su, M. Narayanasamy, S. Angaiah, C. Yan and Q. Peng, *Chem. Eng. J.*, 2020, **399**, 125627.
26 Y. Wen, Z. Wei, J. Liu, R. Li, P. Wang, B. Zhou, X. Zhang, J. Li and Z. Li, *J. Energy Chem.*, 2021, **52**, 412.
27 K. Chu, Y. Liu, Y. Cheng and Q. Li, *J. Mater. Chem. A*, 2020, **8**, 5200.

28 M. Naguib, M. Kurtoglu, V. Presser, J. Lu, J. Niu, M. Heon, L. Hultman, Y. Gogotsi and M. W. Barsoum, *Adv. Mater.*, 2011, **23**, 4248.
29 X. F. Wang, X. Shen, Y. R. Gao, Z. X. Wang, R. C. Yu and L. Q. Chen, *J. Am. Chem. Soc.*, 2015, **137**, 2715.
30 L. Ding, Y. Y. Wei, Y. J. Wang, H. B. Chen, J. Caro and H. H. Wang, *Angew. Chem., Int. Ed.*, 2017, **56**, 1825.
31 J. Liu, H. B. Zhang, R. H. Sun, Y. F. Liu, Z. S. Liu, A. G. Zhou and Z. Z. Yu, *Adv. Mater.*, 2017, **29**, 1702367.
32 M. Alhabeb, K. Maleski, B. Anasori, P. Lelyukh, L. Clark, S. Sin and Y. Gogotsi, *Chem. Mater.*, 2017, **29**, 7633.
33 R. Y. Li, L. B. Zhang, L. Shi and P. Wang, *ACS Nano*, 2017, **11**, 3752.
34 Z. Ling, C. E. Ren, M. Q. Zhao, J. Yang, J. M. Giammarco, J. S. Qiu, M. W. Barsoum and Y. Gogotsi, *Proc. Natl. Acad. Sci. U. S. A.*, 2014, **111**, 16676.
35 J. Zhang, N. Kong, S. Uzun, A. Levitt, S. Seyedin, P. A. Lynch, S. Qin, M. Han, W. Yang, J. Liu, X. Wang, Y. Gogotsi and J. M. Razal, *Adv. Mater.*, 2020, **32**, 2001093.
36 F. Shahzad, A. Iqbal, H. Kim and C. M. Koo, *Adv. Mater.*, 2020, **32**, 2002159.
37 K. Hantanasirisakul and Y. Gogotsi, *Adv. Mater.*, 2018, **30**, 1804779.
38 K. Li, M. Liang, H. Wang, X. Wang, Y. Huang, J. Coelho, S. Pinilla, Y. Zhang, F. Qi, V. Nicolosi and Y. Xu, *Adv. Funct. Mater.*, 2020, **30**, 2000842.
39 M. Yua, S. Zhou, Z. Wang, J. Zhao and J. Qiu, *Nano Energy*, 2018, **44**, 181.
40 F. He, B. Zhu, B. Cheng, J. Yu, W. Ho and W. Macyk, *Appl. Catal., B*, 2020, **362**, 119006.
41 L. Cheng, Q. Chen, J. Li and H. Liu, *Appl. Catal., B*, 2020, **267**, 118379.
42 H. Wang, R. Zhao, J. Qin, H. Hu, X. Fan, X. Cao and D. Wang, *ACS Appl. Mater. Interfaces*, 2019, **11**, 44249.
43 S. Cao, B. Shen, T. Tong, J. Fu and J. Yu, *Adv. Funct. Mater.*, 2018, **28**, 1800136.
44 C. Yang, Q. Tan, Q. Li, J. Zhou, J. Fan, B. Li, J. Sun and K. Lv, *Appl. Catal., B*, 2020, **268**, 118738.
45 M. Naguib, M. Kurtoglu, V. Presser, J. Lu, J. Niu, M. Heon, L. Hultman, Y. Gogotsi and M. W. Barsoum, *Adv. Mater.*, 2011, **23**, 4248.
46 T. Cai, L. Wang, Y. Liu, S. Zhang, W. Dong, H. Chen, X. Yi, J. Yuan, X. Xia, C. Liu and S. Luo, *Appl. Catal., B*, 2018, **239**, 545.
47 P. Koilraj and S. Kannan, *Chem. Eng. J.*, 2013, **234**, 406.
48 G. Zuo, Y. Wang, W. L. Teo, A. Xie, Y. Guo, Y. Dai, W. Zhou, D. Jana, Q. Xian, W. Dong and Y. Zhao, *Chem. Eng. J.*, 2021, **403**, 126328.
49 G. Zuo, Y. Wang, W. L. Teo, A. Xie, Y. Guo, Y. Dai, W. Zhou, D. Jana, Q. Xian, W. Dong and Y. Zhao, *Angew. Chem., Int. Ed.*, 2020, **59**, 11287.
50 Y. Sun, D. Jin, Y. Sun, X. Meng, Y. Gao, Y. Dall'Agnese, G. Chen and X.-F. Wang, *J. Mater. Chem. A*, 2018, **6**, 9124.
51 K. Wang, L. Zhang, Y. Su, D. Shao, S. Zeng and W. Wang, *J. Mater. Chem. A*, 2018, **6**, 8366.
52 X. Liu, J. Liang, X. Song, H. Yang, X. Li, H. Dai, Y. Song, Y. Liu, J. Hu, X. Pan, X. OuYang and Z. Liang, *Chem. Eng. J.*, 2018, **337**, 560.
53 M. Thommes, K. Kaneko, A. V. Neimark, J. P. Olivier, F. Rodriguez-Reinoso, J. Rouquerol and K. S. W. Sing, *Pure Appl. Chem.*, 2015, **87**, 1051.
54 M. Kruk and M. Jaroniec, *Chem. Mater.*, 2001, **13**, 3169.
55 Z. Huang, K. Teramura, H. Asakura, S. Hosokawa and T. Tanaka, *Chem. Sci.*, 2017, **8**, 5797.
56 Q. Han, X. Bai, Z. Man, H. He, L. Li, J. Hu, A. Alsaedi, T. Hayat, Z. Yu, W. Zhang, J. Wang, Y. Zhou and Z. Zou, *J. Am. Chem. Soc.*, 2019, **141**, 4209.
57 X. Li, Y. Sun, J. Xu, Y. Shao, J. Wu, X. Xu, Y. Pan, H. Ju, J. Zhu and Y. Xie, *Nat. Energy*, 2019, **4**, 690.
58 Y. Shen, Q. Han, J. Hu, W. Gao, L. Wang, L. Yang, C. Gao, Q. Shen, C. Wu, X. Wang, X. Zhou, Y. Zhou and Z. Zou, *ACS Appl. Energy Mater.*, 2020, **3**, 6561.
59 A. Ishikawa, T. Takata, J. N. Kondo, M. Hara, H. Kobayashi and K. Domen, *J. Am. Chem. Soc.*, 2002, **124**, 13547.
60 Y. Li, Y. Liu, D. Xing, J. Wang, L. Zheng, Z. Wang, P. Wang, Z. Zheng, H. Cheng, Y. Dai and B. Huang, *Appl. Catal., B*, 2021, **285**, 119855.